MOLECULAR IMAGING AND BIOLOGY

Mol Imaging Biol (2019) 21:1054–1063
DOI: 10.1007/s11307-019-01318-5

Published Online: 25 February 2019

WMIS World Molecular Imaging Society

Check for updates

RESEARCH ARTICLE

Imaging and Characterization of Macrophage Distribution in Mouse Models of Human Prostate Cancer

Ben T. Copeland,[1,2] Hassan Shallal,[1] Chentian Shen,[1] Kenneth J. Pienta,[3] Catherine A. Foss,[1] Martin G. Pomper[1,3]

[1]*The Russell H Morgan Department of Radiology and Radiological Science, Johns Hopkins University School of Medicine, Baltimore, MD, 21287, USA*

[2]*Beckman Research Institute, City of Hope, Duarte, CA, 91010, USA*

[3]*James Buchanan Brady Urological Institute, Johns Hopkins University School of Medicine, Baltimore, MD, 21205, USA*

Abstract

Purpose: Prostate carcinoma consists of tumor epithelium and malignant stroma. Until recently, diagnostic and therapeutic efforts have focused exclusively on targeting characteristics of the tumor epithelium, ignoring opportunities to target inflammatory infiltrate and extracellular matrix components. Prostate tumors are rich in tumor-associated macrophages (TAMs), which can be either of the cytotoxic M1 or protumorigenic M2 phenotype. We have quantified the proportion of each in seven common human prostate tumor lines grown subcutaneously in athymic nude mice and have imaged macrophage densities *in vivo* in xenografts derived from these lines.

Procedures: A panel of seven human prostate cancer xenografts was generated in intact male athymic nude mice reflecting variable expression of the androgen receptor (AR) and prostate-specific membrane antigen (PSMA). Mice were imaged *ex vivo* using near-infrared fluorescence (NIRF) imaging for PSMA expression and total macrophage densities to enable direct comparison between the two. Tumors were harvested for sectioning and additional staining to delineate M1 and M2 phenotype along with vascular density.

Results: Macrophage polarization analysis of sections revealed that all xenografts were > 94% M2 phenotype, and the few M1-polarized macrophages present were confined to the periphery. Xenografts displaying the fastest growth were associated with the highest densities of macrophages while the slowest growing tumors were characterized by focal, tumor-infiltrating macrophage densities. Xenograft sections displayed a strong positive spatial relationship between macrophages, vasculature, and PSMA expression.

Conclusions: Prostate TAM disposition can be imaged *ex vivo* and is associated with growth characteristics of a variety of tumor subtypes regardless of PSMA or AR expression.

Key words: DPA-713, Prognosis, NIRF, Fluorescence imaging

Introduction

Prostate cancer (PC) is the most frequently diagnosed noncutaneous cancer and the second leading cause of cancer-related death in men, representing a predicted

Catherine A. Foss and Martin G. Pomper contributed equally to this work. Electronic supplementary material The online version of this article (https://doi.org/10.1007/s11307-019-01318-5) contains supplementary material, which is available to authorized users.

Correspondence to: Catherine Foss; *e-mail:* cfoss1@jhmi.edu, Martin Pomper; *e-mail:* mpomper@jhmi.edu

164,690 new cases and 29,430 deaths in 2017 [1]. Much progress has been made in the detection of PC, especially with widespread prostate-specific antigen (PSA) testing, which has led to a dramatic rise in identification of local, early stage PC. Mortality rates have been correlatively reduced with PSA testing, although the PSA test has been criticized regarding specificity and sensitivity [2, 3]. It has recently been recognized that positive PSA test results in men later diagnosed with indolent PC have led to overtreatment [4–6]. Accordingly, more accurate ways to distinguish indolent from aggressive PC are needed to suggest appropriate and precise treatment options.

PC is comprised of both tumor and stromal cells, the latter of which can promote the malignant phenotype [7, 8]. To date, efforts at detection of PC in patients have focused almost exclusively on imaging malignant epithelium rather than on the stromal cell component by accessing a variety of targets including the prostate-specific membrane antigen (PSMA) [9, 10], gastrin releasing peptide receptor (GRPR) [11, 12], somatostatin receptors [13], metabolic choline uptake [14], and amino acid transporters using fluciclovine [15] and positron emission tomography (PET). The corresponding imaging agents for each of those targets are fraught with problems related to lack of sensitivity and/or specificity. For example, imaging with radiotracers targeting PSMA demonstrates high specificity, but sensitivity ranging from 33 to 66 % when compared against the gold standard of histopathology [16]. Evidence shows that PSMA imaging may be correlated with the aggressiveness of the tumor detected [17]. New targets are needed for more sensitive detection and which may concurrently inform the biology of the tumor—such as its likelihood to metastasize. The inflammatory cellular component of malignant tissues, specifically tumor-associated macrophages (TAMs), are an integral component of all prostate tumors, regardless of PSMA expression, and represent a new target that may enable sensitive, biologically relevant imaging.

TAMs are positively associated with progression and poor outcome in a number of malignancies [18], including prostate cancer [19–21]. Macrophages of the M2 phenotype predominate over M1 macrophages within malignant lesions. M2 macrophages are associated with wound repair, neovascularization, immunosuppression, and tumor augmentation [22–24] while M1 macrophages are characterized by cytotoxic release of free radicals and tumor suppression. TAMs are present largely at the periphery of tumors and within vascular beds while tumor-infiltrating macrophages (TIMs) are distributed throughout the tumor and are associated with better prognosis in a number of solid tumor types [25, 26]. The distribution of M1 and M2 macrophage densities within PC tumors and specifically within experimental models of PC has not been reported and is the subject of this work. The low molecular weight pyrazolopyrimidines, iodo-DPA-713, and DPA-713-IRDye680LT have previously been shown to target macrophages specifically *in vivo* in preclinical models [27, 28]. Here, we probe macrophage density and spatial distribution using DPA-713-IRDye800CW and near-infrared fluorescence (NIRF) imaging in a panel of experimental models of PC derived from frequently used PC cell lines. We also evaluated the distribution of TAMs within the tumors in relation to PSMA expression and the location of neovasculature and related these parameters to each other and to androgen receptor (AR) expression in an effort to uncover a biomarker related to stroma that may report on the overall malignant potential of the tumor.

Materials and Methods

Cell Lines

C4-2, PC3, DU145, and LAPC-4 cell lines were obtained from the American Type Culture Collection (ATCC, Rockville, MD). $PSMA^+$ PC3-PIP, $PSMA^-$ PC3-flu, and JHU-LNCaP-SM cells were cultured as previously described [29, 30]. All other cell lines were grown in RPMI 1640 media (Mediatech, Manassas, VA) containing 10 % fetal bovine serum (Sigma, St. Louis, MO) and 100 U penicillin/streptomycin antibiotic solution (Mediatech) with the exception of LAPC-4, which was grown in IMDM (Mediatech) with supplements as listed above in addition to containing 1 nM R1881 (Sigma). The cells were subcultured at very low passage in Corning uncoated filter top polystyrene flasks (Sigma) and were maintained at 37 °C in 5 % CO_2 in humidified air. Cells were typically split at 80 % confluence using 0.05 % trypsin (Sigma) in calcium-free Hank's Buffered Salt Solution (Sigma).

Xenograft Models

Animal studies were performed under protocols approved by the Animal Care and Use Committee at Johns Hopkins University. Six-to-eight-week-old male athymic nude mice (NCRNU-M, Taconic, Hudson, NY) were kept in a specific pathogen-free facility under a 12-h day/night cycle with access to standard chow (Teklad 8604 Rodent Diet, Harlan Laboratories, Frederick, MD) and water *ad libitum*. Mice ($n \geq 3$/group) were subcutaneously implanted in the upper left and right axillary flanks with 2×10^6 cells/site for each cell line (except LAPC-4 which utilized 4×10^6 cells/site) in 50 μl of Hank's Buffered Salt Solution (Beckton-Dickenson, Franklin Lakes, NJ). JHU-LNCaP-SM and LAPC-4 cells were inoculated 1:1 (*v*:*v*) with Matrigel® (Sigma) in Hank's Buffered Salt Solution. A 60-day slow release testosterone pellet (Innovative Research of America, Sarasota, FL) was subcutaneously implanted in the mid-dorsal flank of the LAPC-4 xenograft models at the time of engraftment. Once tumors reached approximately 1000 mm^2, they were excised and immediately imaged, enabling comparison of tumor dimensions with time needed to reach those dimensions.

Ex vivo NIRF Imaging

When tumor xenografts reached approximately 4–6 mm in diameter, 1 nmol of YC-XI-46-Cy5.5 (PSMA-specific, [31]) and 8 nmol of DPA-713-IRDye800CW (US 20150044141 A1) (macrophage-specific) agents were co-injected intravenously in PBS, pH 7.5. At 24 h post-injection, the animals were euthanized by isoflurane-anesthetized cervical dislocation and dissected to expose completely the subcutaneous flank tumors in context with the rest of the ventral body. The carcasses were then photographed using the visible, 680/710 and 790/800 nm excitation/emission filters using a Pearl Impulse Small Animal Imager (LI-COR, Lincoln, NE). Images were processed and displayed using the manufacturer's software (Pearl Impulse Software, v. 2.0). Color bars represent relative optical units.

Tumor xenografts and selected lymph nodes were harvested and immediately frozen over dry ice and stored at −80 °C until sectioning to 20 μm thicknesses using a Microm® HM 550 cryotome (Thermo Scientific, Waldorf, Germany) and adhered to charged glass slides (VWR, Radnor, PA). As indicated, some tissue sections containing either co-injected YC-XI-46-Cy5.5 and DPA-713-IRDye800CW, or sections devoid of injected agents and subsequently probed with anti-CD68-IRDye680RD and anti-CD206-IRDye800CW, were scanned using the same channels as above, minus visible light, using a Li-COR Odyssey scanner. Images were displayed and analyzed using the Odyssey v. 3.0 software (LI-COR). Fluorescent anti-CD68 (Abcam, Cambridge, UK, ab53444) and anti-CD206 (Abcam, ab64693) were labeled as follows: 100 μg of each antibody was dissolved in 100 μl of PBS, pH 7.4 in a microcentrifuge tube. One microliter of a stock solution of IRDye680RD or IRDye800CW, as indicated, (50 mg/mL in DMSO, LI-COR Biosciences, Lincoln, NE) was then added to the antibody solution and the labeling reaction proceeded at ambient temperature for 12 min. Unincorporated dye was removed using Sephadex G-25 size exclusion columns. Antibody purity was tested using Whatman 60 Å silica thin layer chromatography (Sigma-Aldrich) developed in acetonitrile with UV detection (radiochemical purity ≥ 95 %).

Histopathology and Multispectral Immunoepifluorescence

A subset of the collected tissues were fixed in formalin, embedded in paraffin and sectioned to 4 μm onto charged glass slides, and hematoxylin and eosin (H&E) stains were performed according to the manufacturer's protocol (BBC Biochemical, Washington, DC). Frozen sections were equilibrated at ambient temperature for 10 min and then rinsed briefly in acetone prior to washing twice in PBS for 5 min. The sections were then co-probed over 1 h at ambient temperature with rat anti-CD68 (Abcam, ab53444), mouse anti-PSMA (Abcam, ab66912), and rat anti-CD31 conjugated to phycoerythrin (PE) (Abcam, ab25644). All antibodies were used at 14 μg/mL in PBS, pH 7.5 containing 10 % fetal bovine serum (FBS, Gibco, Grand Island, NY). Slides were then washed twice in PBS for 5 min and anti-CD68 was detected using anti-rat-FITC (Invitrogen; 1:200) and anti-PSMA detected with anti-mouse AlexaFluor® 680 (Invitrogen; 1:200) secondary antibodies for 30 min at ambient temperature. Slides were then incubated with Hoechst 33342 for 1.5 min (Invitrogen; 1:1000 in PBS) and subsequently washed twice in PBS for 5 min followed by mounting with aqueous mounting medium (Dako, Carpenteria, CA) and a cover-slip. The slides were viewed using a Nikon 80i upright microscope (Nikon Instruments, Melville, NY) equipped with a Nikon DS-Qi1Mc darkfield CCD camera and images were processed using the Nikon Basic Elements Imaging Software. Quantification of M1 and M2 macrophages was accomplished using a LI-COR Biosciences Odyssey scanner with the manufacturer's software performing whole mount pixel counting in each relevant channel over four sections per tumor type. Two tumors were used from each tumor type for counting.

Results

Accumulation of DPA-713-IRDye800CW Is Positively Correlated with TAM Densities and Tumor Xenograft Growth Rate

We evaluated the ability of DPA-713-IRDye800CW to detect TAM densities *in vivo* and *ex vivo* within a range of prostate tumor xenografts reflecting divergent AR and PSMA expression status (Table 1). PC3 [AR-, androgen insensitive (AI) and PSMA-]; PC3-PIP (AR-, AI and $PSMA_{high}$); PC3-flu (AR-, AI and PSMA-); DU145 (AR-, AI and PSMA-); LAPC-4 (AR+, AS_{high} and PSMA+); C4–2 (AR_{mut}+, AI and PSMA+); and JHU-LNCaP-SM [32] (AR_{mut}+, AI and PSMA+) were used. All seven tumor xenografts exhibited high contrast uptake of the imaging agent within a background of surrounding healthy tissues and were readily visualized regardless of AR expression or sensitivity (Fig. 1). The intensity and spatial distribution of DPA-713-IRDye800CW uptake within tumor showed a trend of increased total DPA-713-IRDye800CW uptake within faster growing tumors (Fig. 1, top panels) while slower growing tumors contained less imaging agent and demonstrated a more punctate pattern (Fig. 1, lower panels). Both adjacent and distant enlarged and inflamed lymph nodes could also be visualized by DPA-713-IRDye800CW (Fig. 1, yellow arrows). There was also presence of the imaging agent within liver and the urinary tract due to metabolism and clearance (Fig. 1L, U). YC-XI-46-Cy5.5, a fluorescent imaging agent specific for PSMA [31], readily identified tumor xenografts expressing PSMA while DPA-713-IRDye800CW exhibited high contrast from TAM densities present in all xenograft lines regardless of PSMA expression status (Fig. 2).

Table 1. Cell lines, androgen receptor status, PSMA expression, and tumor growth

Cell line	Androgen receptor status	PSMA expression	Xenograft growth rate
PC-3	Negative	Negative	Rapid
PC-3 PIP	Negative	High	Rapid
PC-3 flu	Negative	Negative	Rapid
DU145	Negative	Negative	Moderate
LAPC4	Positive, WT, AS	Moderate	Moderate
JHU-LNCaP-SM	Positive, mutant, AI	Low	Moderate
C4-2	positive, mutant, AI	High	Moderate

WT wild-type, *AS* androgen sensitive, *AI* androgen independent

The Spatial Localization of DPA-713-IRDye800CW Uptake in Tumor Xenograft Lines Correlates with Tumor Growth Rate

DPA-713-IRDye800CW displayed a distinct and varied uptake pattern within tumor xenografts according to cell line and growth rate (Fig. 3). Faster growing tumors (2×10^6 inoculated cells to 4–6 mm diameter xenograft in ≤ 2 weeks: PC3, PC3-flu, and PC3-PIP) displayed probe uptake mostly at the tumor rim while the slower growing, less aggressive tumor types ($2–4 \times 10^6$ inoculated cells to 4–6 mm diameter xenograft in 3–8 weeks, respectively: C4-2 and LAPC-4) displayed DPA-713-IRDye800CW uptake in a discrete, focal pattern within the tumor parenchyma. The two tumors observed to have intermediate growth (size) (JHU-LNCaP-SM and DU145) displayed probe uptake that distributed both at the tumor rim and within the parenchyma. Overlay with YC-XI-46-Cy5.5 (PSMA, green) revealed a non-overlapping distribution pattern among PSMA-expressing tumors, indicating both epidermal and stromal localization of

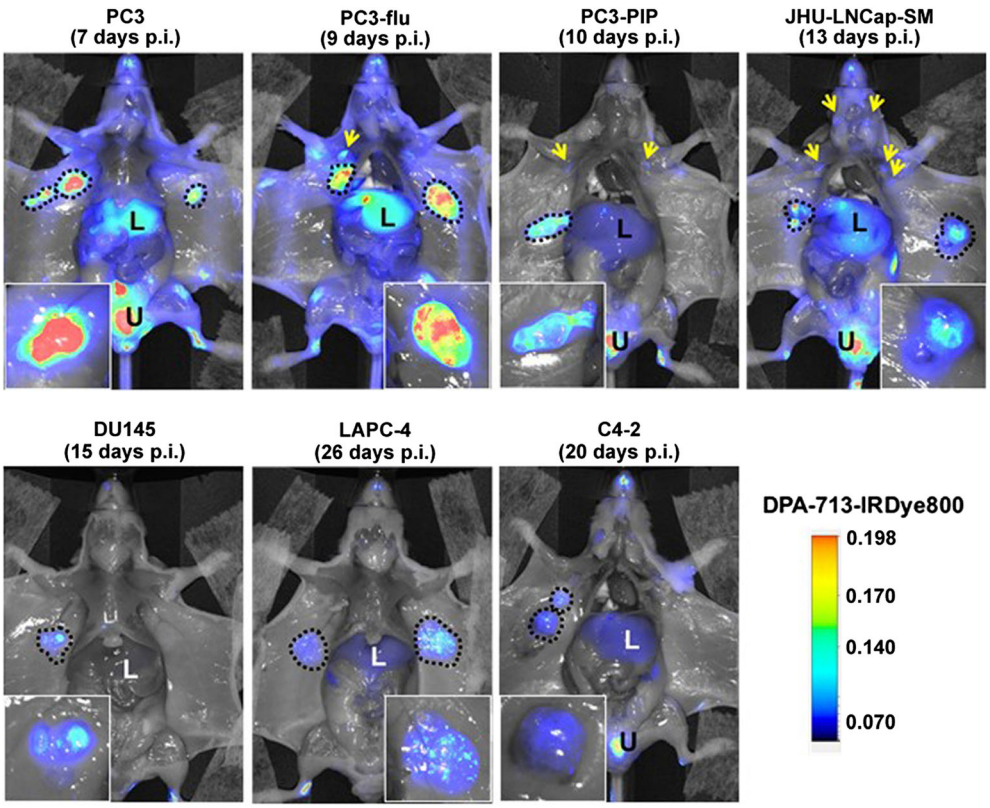

Fig. 1. Macrophage-specific DPA-713-IRDye800CW accumulation in tumor xenografts is proportional to tumor growth rate. Seven different subcutaneous xenograft models were generated in intact male athymic nude mice and were injected with an identical quantity of fluorescent probe. Images are normalized to the same exposure time and reveal relative macrophage densities according to both tumor lineage and xenograft size. Uptake of fluorescent probe is also observed in the brachial, axillary, and superficial cervical lymph nodes (yellow arrows), while the liver (L) and urinary tract (U) represent metabolic clearance. Post-inoculation (p.i) represents time from tumor cell inoculation to time of imaging. A scale bar represents relative fluorescence units. Images were obtained at 24 h after injection of DPA-713-IRDye800CW.

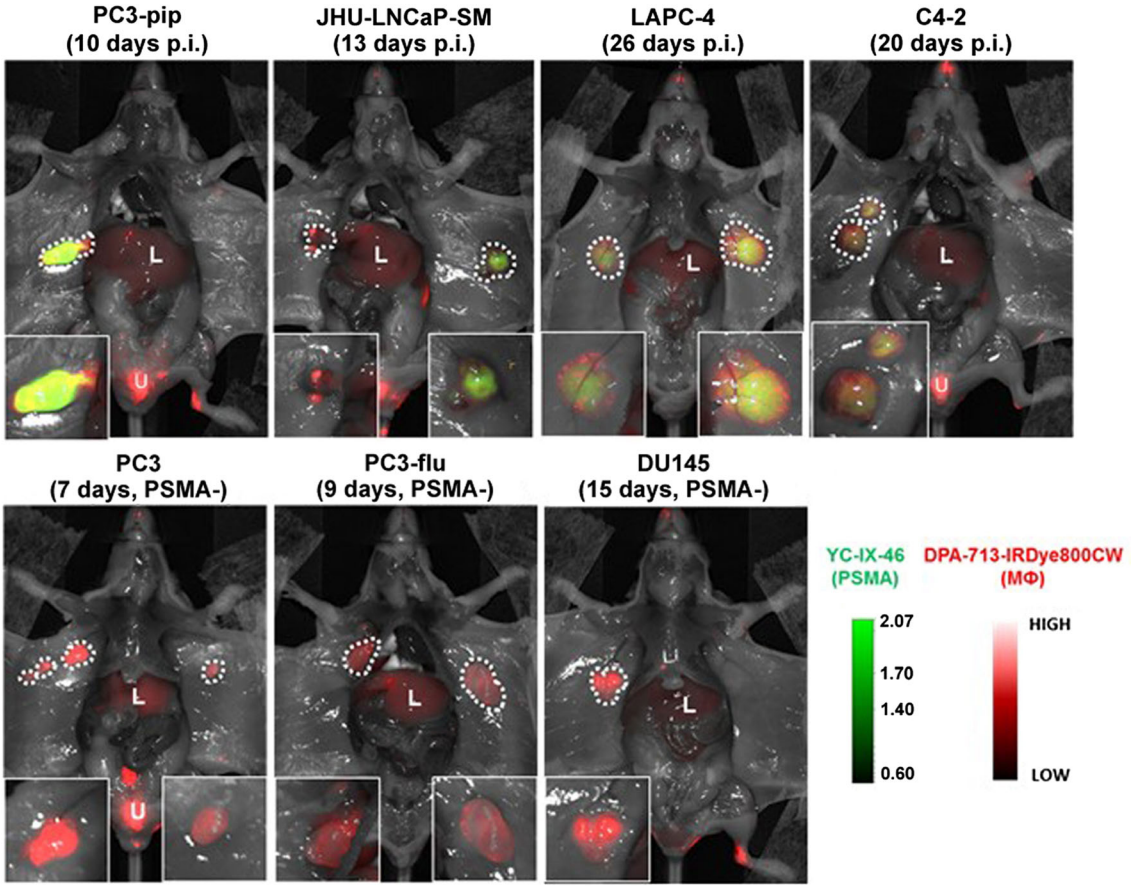

Fig. 2. Macrophage density and spatial location are readily detected in all tumor xenografts regardless of PSMA expression. All seven xenograft models were concurrently imaged using NIRF for macrophage densities (DPA-713-IRDye800CW) and PSMA expression (YC-IX-46). All PSMA-expressing tumors were readily detected with the PSMA-specific probe while all xenograft types were delineated using the macrophage-specific fluorescent probe. Post-inoculation (p.i) represents time from tumor graft inoculation to time of imaging. L, liver and U, urinary bladder, both of which display metabolic clearance of probes. YC-IX-46 intensity is normalized to the same exposure time while DPA-713-IRDye800CW intensity is normalized to liver intensity in all mice.

TAMs. Additionally, a weak signal observed from YC-XI-46-Cy5.5 (Fig. 3, blue) in PSMA non-expressing tumors (PC3 lines, DU145) suggested the presence of PSMA+ neovasculature [33], which strongly colocalized with DPA-713-IRDye800CW distribution largely at the tumor rim.

Tumor Infiltrating Macrophages Are Almost Entirely of the M2 Phenotype

Whole mount xenograft tumor sections from each cell line were probed with both anti-CD68 antibody (pan-macrophage) and anti-CD206 antibody (M2 phenotype) [34] to delineate total and M2 phenotype macrophages across representative tumor xenograft sections (Fig. 4a–c). 94–100 % of cells in the tumor parenchyma in each tumor line that stained positive for CD68 also stained positive for CD206 (Fig. 4d), indicating nearly universal polarization of TAMs to the alternatively activated M2, protumor phenotype.

Macrophages and PSMA+ Epithelium Are Spatially Associated with Tumor Vasculature

The xenograft microenvironment in each tumor type was further characterized for spatial distributions of CD68 expressing macrophages and PSMA-expressing cells relative to CD31, which is a marker of endothelial vasculature. Within all seven xenograft types, macrophages were closely associated with blood vessels (Fig. 5) with the majority of macrophages located within 60 μm of CD31 positive vasculature. PSMA expression was also observed to be enriched adjacent to sites of vascularization in addition to lower basal expression observed throughout the tumor parenchyma (Fig. 5 and Suppl. Figs. 2–8 (in Electronic

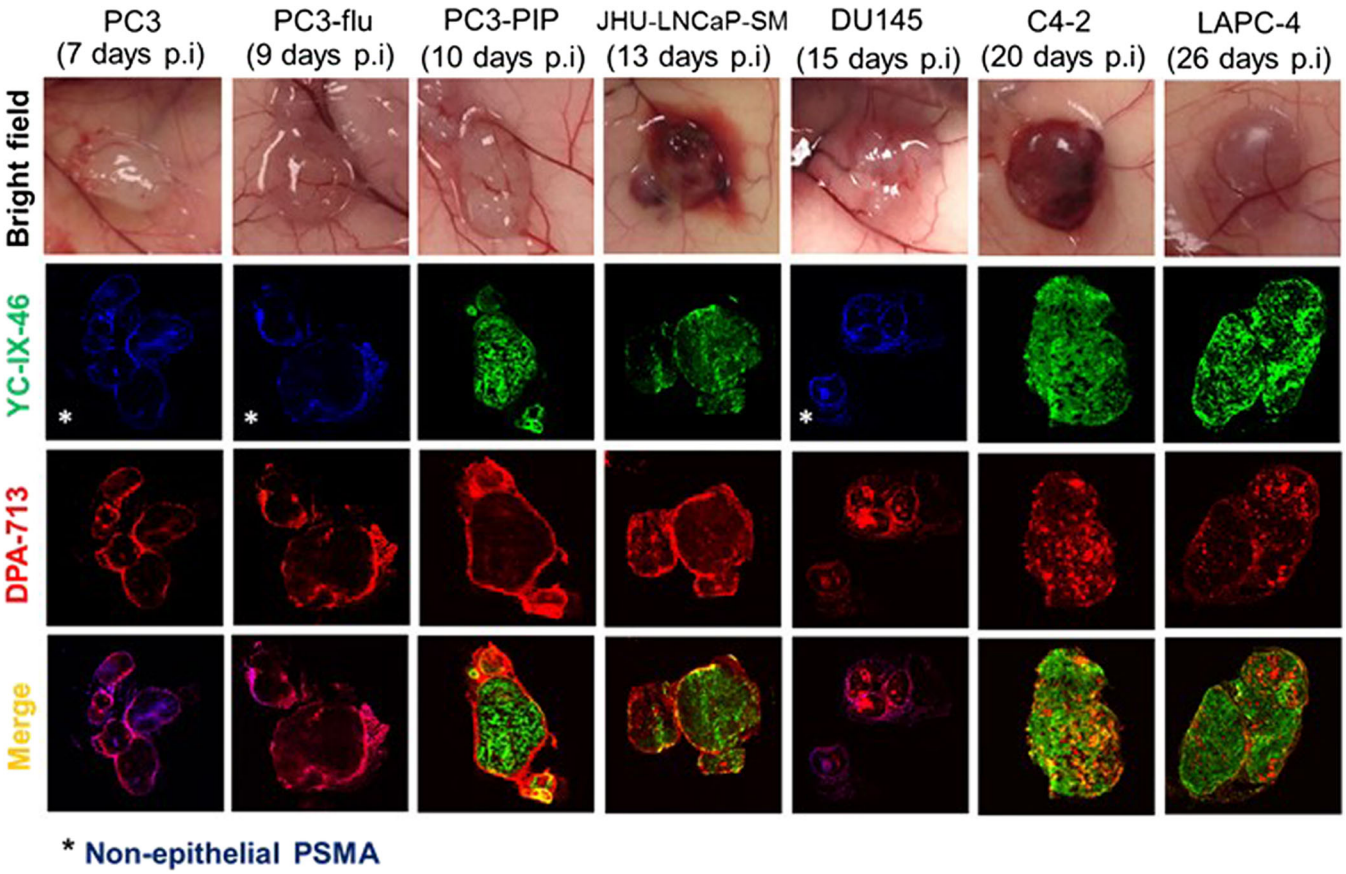

Fig. 3. Localization of macrophage density correlates with tumor growth rate. Whole mount tumor sections derived from Fig. 2 were imaged *ex vivo* with residual DPA-713-IRDye800CW (Mϕ) and YC-IX-46 (PSMA). Macrophage density was primarily localized to either the tumor capsule (fast growing tumors) or distributed as inclusions within the tumor parenchyma (slower growing tumors) or a combination (JHU-LNCaP-SM). PSMA expression was found to be evenly distributed in all PSMA+ tumors except for JHU-SM-LNCaP. Low-intensity PSMA expression was detected (blue) primarily in the peritumoral rim of PSMA-null tumor lines and colocalized with signal from the macrophage probe, suggesting the presence of PSMA+ neovasculature. All images are scaled separately for each probe to highlight spatial localization of macrophage density and PSMA expression in each tumor section. NB: the YC-IX-46 intensity was overly enhanced for the PSMA-expressing tumor types to show low PSMA expression in tumor neovascularization and the brightfield image of the PC3 tumor is not the same tumor that was subsequently characterized.

Supplementary Material) showing each pseudocolor channel separately).

Discussion

We report the distribution of macrophages in seven common human prostate tumor lines grown subcutaneously in male athymic nude mice. The cell lines chosen reflect different AR status and sensitivity, PSMA expression, and PSA expression, three biomarkers currently used to predict aggressiveness [35, 36]. DPA-713-IRDye800CW is a red-shifted fluorescent analog of DPA-713-IRDye680LT, specific for CD68-expressing phagocytic cells and has been used to detect macrophage densities in mice engrafted with the abovementioned PC cell lines [27, 28, 37]. In summary, *in vivo* DPA-713-IRDye800CW accumulation was proportional to xenograft growth rate, the amount of time xenografts took to reach ~1000 mm^3 [38], in mice. DPA-713-IRDye800CW detected all xenografts regardless of PSMA expression. The spatial localization of DPA-713-IRDye800CW deposition correlated to tumor growth rate. Greater than 94 % of all TAMs in xenograft sections were of the M2 phenotype and immunofluorescence microscopy revealed that macrophages were closely associated with vasculature and PSMA-expressing epithelium in all tumors.

In normal human prostate cells PSMA is expressed and localized in the cytoplasm and apical side of the epithelium [39]. During neoplastic transformation, PSMA transfers from the apical membrane to the luminal surface of the ducts [40]. Additionally, PSMA expression levels increase according to the stage and Gleason grade of the lesion [41, 42]. Those biological characteristics make PSMA an attractive target for theranostics targeting prostate cancer. Although the majority of prostate adenocarcinomas, including primary and lymph node metastatic lesions, express PSMA, an early report indicated that nearly 60 % of bone

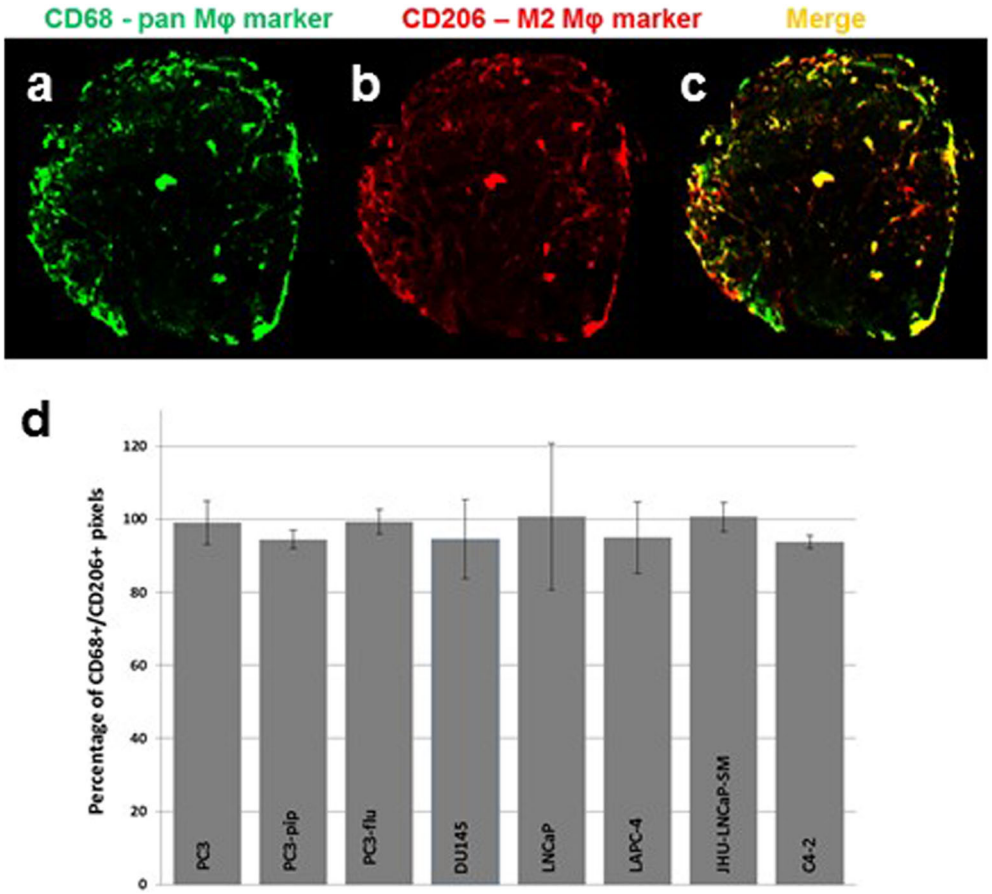

Fig. 4. Macrophages in the tumor parenchyma display a mostly M2 phenotype. Whole mount tumor xenograft sections were stained for **a** anti-CD68 antibody (pan-macrophage, green) and **b** anti-CD206 (M2 Mϕ marker in red) with **c** an overlay shown. **d** Analysis software was used to separate the channels for each antibody and quantitate intensities. All xenograft types display between 94 and 100 % of an M2 phenotype in the tumor parenchyma. Error bars represent standard deviation among the average of the sections counted.

metastatic lesions did not demonstrate substantial PSMA expression [42]. In the current study, we found that DPA-713-IRDye800CW detected all tumors regardless of PSMA expression. That is important due to the fact that over 8 % of human prostatic adenocarcinomas do not express PSMA but still have an unfavorable prognosis on par with patients harboring PSMA-expressing lesions [43, 44]. Additionally, current noninvasive methods to detect PSMA-expressing tumors range in sensitivity from 10 to 99 %, depending on tissue location, imaging agent, and modality [45–47]. Small cell carcinomas of the prostate, originating from neuroendocrine stem cells, also do not express PSMA, and these tumors have no tissue-specific surface-accessible biomarkers [48].

TAMs can be detected in all PC and increased density of TAMs is also associated with poor prognosis [49]. Gollapudi, et al. stained for CD68, a TAM marker, in prostatectomy specimens from 332 patients and found that the mean TAM number was higher in higher grade PC [20]. Lanciotti, et al. reported that 63.4 % of all patients showed an M2 phenotypic prevalence and patients with a higher density of TAMs had a worse prognosis. In that instance, a predominant M2 phenotype was associated with tumor extension [19]. Accordingly, TAMs and PSMA are both associated with progression of PC [50]. However, the biological relationship between PSMA expression and TAM infiltration has not been elucidated. Data exist showing pro-inflammatory signaling by PSMA through MAPK pathways in cancer cells to generate pro-inflammatory cytokines [51], which recruit and phenotypically influence leukocytes. Our results revealed that TAMs were closely associated with new vasculature in all tumor xenografts as well as having displayed a tropism toward PSMA-expressing epithelium in xenografts with both homogeneous and heterogeneous expression of PSMA.

TAMs which are abundantly found in prostate cancer [19] can create an immunosuppressive tumor microenvironment reducing the therapeutic efficacy of checkpoint therapies, such as anti-CTLA-4 and anti-PD-1/PD-L1 antibodies through suppression of effector T cell activation [52]. Furthermore, cancer stem cells (CSCs) have been associated with resistance to androgen deprivation therapy and PC

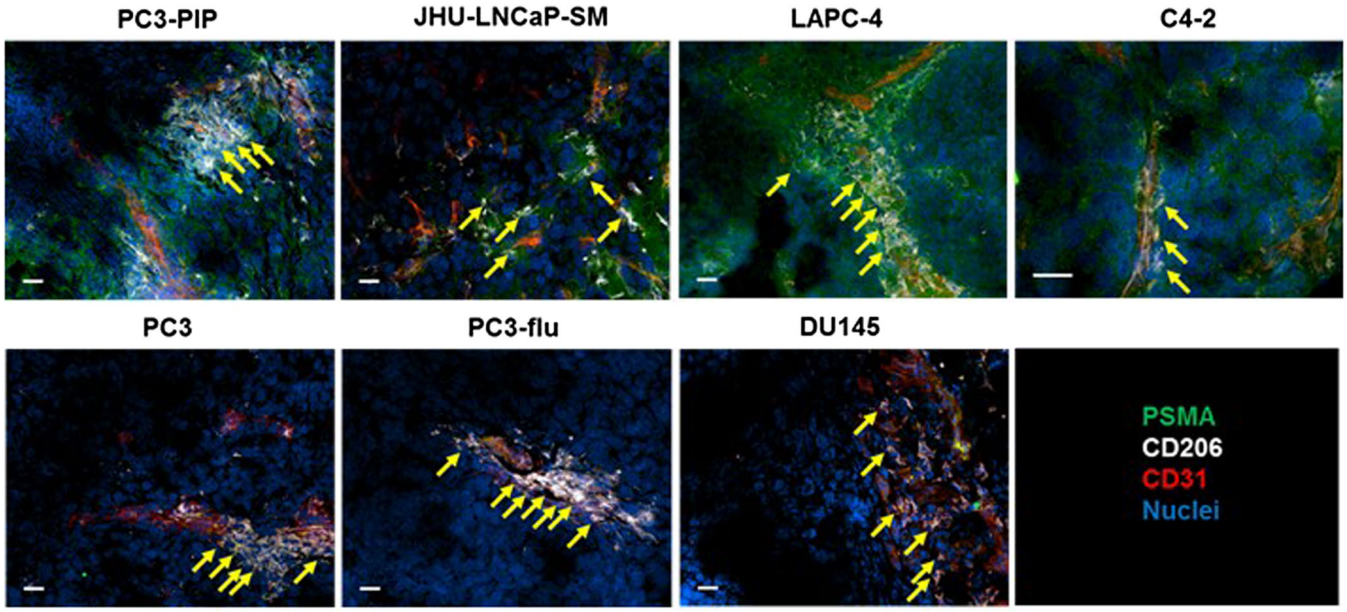

Fig. 5. CD206+ macrophages and PSMA+ cells are closely proximally associated with vasculature (CD31) in all seven xenograft lines. Frozen sections were probed with anti-CD206, anti-PSMA, and anti-CD31 antibodies. CD206+ cells (yellow arrows) were closely associated with CD31 in all xenografts types. PSMA+ cells were also enriched at sites of CD31+ vasculature the parenchymal epithelium within PSMA+ tumor xenografts. Scale bar = 50 μm.

progression through recruitment of monocytes and polarization to TAMs [53]. Thus, imaging modalities targeting TAMs, such as [^{124}I]iodo-DPA-713 PET have promising potential to help identify higher probability of success in these therapies in high TAMs burden cases.

Because of the abovementioned clinical significance of identifying TAMs, a variety of imaging agents has been developed to detect TAMs *in vivo* using different preclinical cancer models. Macrophage mannose receptor (MMR; CD206) is commonly used as a target for mature macrophages. Sun, et al. conjugated anti-mouse CD206 antibody with DyLight680 to generate a CD206-targeting NIRF agent (dye-anti-CD206) and their results demonstrated that NIRF imaging using this agent would allow noninvasive visualization of TIMs *in vivo* in a breast cancer mouse model [54]. Movahedi, et al. developed Tc-99 m labeled anti-CD206 nanobodies to imaging TAMs in solid tumor models by using single-photon emission computed tomography [55]. In addition, different nanoparticles were also investigated for TAM-targeted imaging [56, 57]. Pérez-Medina, et al. described the development of reconstituted high-density lipoprotein (rHDL)-facilitated TAM PET imaging in a breast cancer model [57]. We report here a readily translatable (*via* analogous [^{124}I]iodo-DPA-713 PET) targeted imaging agent for TAMs in experimental models of human prostate cancer using a small-molecule NIRF probe. Compared with antibodies and nanoparticles, DPA-713 analogs are targeted only toward cells of macrophage lineage, are cleared quickly from the bloodstream, have low antigenic potential and display low background activity including low healthy liver uptake [58].

Conclusion

DPA-713-IRDye800CW was universally retained by all PC xenografts tested *in vivo* regardless of PSMA or AR expression and this retention reflected selective trapping by CD68-expressing phagocytes. TAM accumulation was highest near epithelial and presumptive endothelial [33, 44, 59] tumor PSMA expression, especially at sites of vascular sprouting. Macrophage imaging with analogs of DPA-713 may help identify all solid PC, characterize their inflammatory phenotype, and possibly delineate rapid from slower growing disease.

Acknowledgments. We thank Ying Chen for provision of YC-XI-46-Cy5.5.

Funding Information. This study is supported by CA134675, CA184228, EB024495 and the anonymous donor through the James Buchanan Brady Urological Institute who, in part, funded this work.

Compliance with Ethical Standards

Conflict of Interest

CAF and MGP hold a share in patent PCT/US13/31461 “Synthesis And Application Of Novel Imaging Agents Conjugated To DPA 713 Analogs For Imaging Inflammation” and MGP holds a share in US20120009121A1 “PSMA-targeting compounds and uses thereof”. All other authors declare no conflict of interest.

References

1. Siegel RL, Miller KD, Jemal A (2017) Cancer statistics, 2017. CA Cancer J Clin 67:7–30
2. Hugosson J, Carlsson S, Aus G, Bergdahl S, Khatami A, Lodding P, Pihl CG, Stranne J, Holmberg E, Lilja H (2010) Mortality results from the Goteborg randomised population-based prostate-cancer screening trial. Lancet Oncol 11:725–732
3. Schroder FH, Hugosson J, Roobol MJ et al (2012) Prostate-cancer mortality at 11 years of follow-up. N Engl J Med 366:981–990
4. Jemal A, Fedewa SA, Ma J, Siegel R, Lin CC, Brawley O, Ward EM (2015) Prostate cancer incidence and PSA testing patterns in relation to USPSTF screening recommendations. JAMA 314:2054–2061
5. Harris R, Lohr KN (2002) Screening for prostate cancer: an update of the evidence for the U.S. Preventive Services Task Force. Ann Intern Med 137:917–929
6. Schröder FH, Hugosson J, Roobol MJ, Tammela TL, Ciatto S, Nelen V, Kwiatkowski M, Lujan M, Lilja H, Zappa M, Denis LJ, Recker F, Páez A, Määttänen L, Bangma CH, Aus G, Carlsson S, Villers A, Rebillard X, van der Kwast T, Kujala PM, Blijenberg BG, Stenman UH, Huber A, Taari K, Hakama M, Moss SM, de Koning HJ, Auvinen A, ERSPC Investigators (2012) Prostate-cancer mortality at 11 years of follow-up. New Engl J Med 366:981–990
7. Krušlin B, Ulamec M, Tomas D (2015) Prostate cancer stroma: an important factor in cancer growth and progression. Bosnian J Basic Med Sci 15:1–8
8. Packer JR, Maitland NJ (2016) The molecular and cellular origin of human prostate cancer. BBA - Mol Cell Res 1863:1238–1260
9. Bouchelouche K, Choyke PL (2016) Prostate-specific membrane antigen positron emission tomography in prostate cancer: a step toward personalized medicine. Curr Opin Oncol 28:216–221
10. Maurer T, Eiber M, Schwaiger M, Gschwend JE (2016) Current use of PSMA-PET in prostate cancer management. Nat Rev Urol 13:226–235
11. Carlucci G, Kuipers A, Ananias HJ et al (2015) GRPR-selective PET imaging of prostate cancer using [^{18}F]-lanthionine-bombesin analogs. Peptides 67:45–54
12. Liu Y, Hu X, Liu H, Bu L, Ma X, Cheng K, Li J, Tian M, Zhang H, Cheng Z (2013) A comparative study of radiolabeled bombesin analogs for the PET imaging of prostate cancer. J Nucl Med 54:2132–2138
13. Morgat C, Mishra AK, Varshney R, Allard M, Fernandez P, Hindie E (2014) Targeting neuropeptide receptors for cancer imaging and therapy: perspectives with bombesin, neurotensin, and neuropeptide-Y receptors. J Nucl Med 55:1650–1657
14. Schlenter M, Berneking V, Krenkel B, Mottaghy FM, Vögeli TA, Eble MJ, Pinkawa M (2018) Intensity-modulated radiotherapy of prostate cancer with simultaneous integrated boost after molecular imaging with ^{18}F-choline-PET/CT : clinical results and quality of life. Strahlenther Onkol 194:638–645
15. Parent EE, Schuster DM (2018) Update on ^{18}f-fluciclovine PET for prostate cancer imaging. J Nucl Med 59(5):733–739
16. Budaus L, Leyh-Bannurah SR, Salomon G et al (2016) Initial experience of ^{68}Ga-PSMA PET/CT imaging in high-risk prostate cancer patients prior to radical prostatectomy. Eur Urol 69:393–396
17. Kiess AP, Banerjee SR, Mease RC, Rowe SP, Rao A, Foss CA, Chen Y, Yang X, Cho SY, Nimmagadda S, Pomper MG (2015) Prostate-specific membrane antigen as a target for cancer imaging and therapy. Q J Nucl Med Mol Imaging 59:241–268
18. Bingle L, Brown NJ, Lewis CE (2002) The role of tumour-associated macrophages in tumour progression: implications for new anticancer therapies. J Pathol 196:254–265
19. Lanciotti M, Masieri L, Raspollini MR et al (2014) The role of M1 and M2 macrophages in prostate cancer in relation to extracapsular tumor extension and biochemical recurrence after radical prostatectomy. Biomed Res Int 2014:6
20. Gollapudi K, Galet C, Grogan T, Zhang H, Said JW, Huang J, Elashoff D, Freedland SJ, Rettig M, Aronson WJ (2013) Association between tumor-associated macrophage infiltration, high grade prostate cancer, and biochemical recurrence after radical prostatectomy. Am J Cancer Res 3:523–529
21. Hu W, Qian Y, Yu F et al (2015) Alternatively activated macrophages are associated with metastasis and poor prognosis in prostate adenocarcinoma. Oncol Lett 10:1390–1396
22. Qian B-Z, Pollard JW (2010) Macrophage diversity enhances tumor progression and metastasis. Cell 141:39–51
23. Quail DF, Joyce JA (2013) Microenvironmental regulation of tumor progression and metastasis. Nat Med 19:1423–1437
24. Squadrito M, De Palma M (2011) Macrophage regulation of tumor angiogenesis: implications for cancer therapy. Mol Asp Med 32:123–145
25. Dai F, Liu L, Che G, Yu N, Pu Q, Zhang S, Ma J, Ma L, You Z (2010) The number and microlocalization of tumor-associated immune cells are associated with patient's survival time in non-small cell lung cancer. BMC Cancer 10:220
26. Kawai O, Ishii G, Kubota K, Murata Y, Naito Y, Mizuno T, Aokage K, Saijo N, Nishiwaki Y, Gemma A, Kudoh S, Ochiai A (2008) Predominant infiltration of macrophages and CD8+ T cells in cancer nests is a significant predictor of survival in stage IV nonsmall cell lung cancer. Cancer 113:1387–1395
27. Foss CA, Harper JS, Wang H, Pomper MG, Jain SK (2013) Noninvasive molecular imaging of tuberculosis-associated inflammation with radioiodinated DPA-713. J Infect Dis 208:2067–2074
28. Foss CA, Bedja D, Mease RC, Wang H, Kass DA, Chatterjee S, Pomper MG (2015) Molecular imaging of inflammation in the ApoE -/- mouse model of atherosclerosis with IodoDPA. Biochem Biophys Res Commun 461:70–75
29. Banerjee SR, Foss CA, Castanares M, Mease RC, Byun Y, Fox JJ, Hilton J, Lupold SE, Kozikowski AP, Pomper MG (2008) Synthesis and evaluation of technetium-99m- and rhenium-labeled inhibitors of the prostate-specific membrane antigen (PSMA). J Med Chem 51:4504–4517
30. Castanares MA, Copeland BT, Chowdhury WH et al (2015) Characterization of a novel metastatic prostate cancer cell line of LNCaP origin. Prostate. https://doi.org/10.1002/pros.23115
31. Chen Y, Pullambhatla M, Banerjee SR, Byun Y, Stathis M, Rojas C, Slusher BS, Mease RC, Pomper MG (2012) Synthesis and biological evaluation of low molecular weight fluorescent imaging agents for the prostate-specific membrane antigen. Bioconjug Chem 23:2377–2385
32. Castanares MA, Copeland BT, Chowdhury WH, Liu MM, Rodriguez R, Pomper MG, Lupold SE, Foss CA (2016) Characterization of a novel metastatic prostate cancer cell line of LNCaP origin. Prostate 76:215–225
33. Grant CL, Caromile LA, Ho V, Durrani K, Rahman MM, Claffey KP, Fong GH, Shapiro LH (2012) Prostate specific membrane antigen (PSMA) regulates angiogenesis independently of VEGF during ocular neovascularization. PLoS One 7:e41285
34. Klar AS, Michalak-Mićka K, Biedermann T, Simmen-Meuli C, Reichmann E, Meuli M (2018) Characterization of M1 and M2 polarization of macrophages in vascularized human dermo-epidermal skin substitutes in vivo. Pediatr Surg Int 34:129–135
35. Segawa N, Mori I, Utsunomiya H, Nakamura M, Nakamura Y, Shan L, Kakudo K, Katsuoka Y (2001) Prognostic significance of neuroendocrine differentiation, proliferation activity and androgen receptor expression in prostate cancer. Pathol Int 51:452–459
36. Dunsmuir WD, Gillett CE, Meyer LC et al (2000) Molecular markers for predicting prostate cancer stage and survival. BJU Int 86:869–878
37. Ordonez AA, Pokkali S, DeMarco VP et al (2014) Radioiodinated DPA-713 imaging correlates with bactericidal activity of tuberculosis treatments in mice. Antimicrob Agents Chemother 59:642–649
38. Cunningham D, You Z (2015) In vitro and in vivo model systems used in prostate cancer research. J Biol Methods 2:17. https://doi.org/10.14440/jbm.2015.63
39. DeMarzo AM, Nelson WG, Isaacs WB, Epstein JI (2003) Pathological and molecular aspects of prostate cancer. Lancet 361:955–964
40. Huang E, Teh BS, Mody DR, Carpenter LS, Butler EB (2003) Prostate adenocarcinoma presenting with inguinal lymphadenopathy. Urology 61:463
41. Bostwick DG, Pacelli A, Blute M, Roche P, Murphy GP (1998) Prostate specific membrane antigen expression in prostatic intraepithelial neoplasia and adenocarcinoma: a study of 184 cases. Cancer 82:2256–2261
42. Silver DA, Pellicer I, Fair WR, Heston WD, Cordon-Cardo C (1997) Prostate-specific membrane antigen expression in normal and malignant human tissues. Clin Cancer Res 3:81–85
43. Schlomm T, Petersen A, Hellwinkel O et al (2007) Alterations of the physiological PSMA expression patterns are associated with poor prognosis in prostate cancer. Cancer Res 67:160

44. Caromile LA, Dortche K, Rahman MM, Grant CL, Stoddard C, Ferrer FA, Shapiro LH (2017) PSMA redirects cell survival signaling from the MAPK to the PI3K-AKT pathways to promote the progression of prostate cancer. Sci Signal 10(470). https://doi.org/10.1126/scisignal.aag3326.
45. Su HC, Zhu Y, Ling GW, Hu SL, Xu XP, Dai B, Ye DW (2017) Evaluation of 99mTc-labeled PSMA-SPECT/CT imaging in prostate cancer patients who have undergone biochemical relapse. Asian J Androl 19:267–271
46. Pyka T, Okamoto S, Dahlbender M, Tauber R, Retz M, Heck M, Tamaki N, Schwaiger M, Maurer T, Eiber M (2016) Comparison of bone scintigraphy and ^{68}Ga-PSMA PET for skeletal staging in prostate cancer. Eur J Nucl Med Mol Imaging 43:2114–2121
47. Rowe SP, Gorin MA, Hammers HJ, Pomper MG, Allaf ME, Javadi MS (2016) Detection of ^{18}F-FDG PET/CT occult lesions with 18F-DCFPyL PET/CT in a patient with metastatic renal cell carcinoma. Clin Nucl Med 41:83–85
48. Sun Y, Niu J, Huang J (2009) Neuroendocrine differentiation in prostate cancer. Am J Transl Res 1:148–162
49. Nonomura N, Takayama H, Nakayama M, Nakai Y, Kawashima A, Mukai M, Nagahara A, Aozasa K, Tsujimura A (2011) Infiltration of tumour-associated macrophages in prostate biopsy specimens is predictive of disease progression after hormonal therapy for prostate cancer. BJU Int 107:1918–1922
50. Kaittanis C, Andreou C, Hieronymus H, Mao N, Foss CA, Eiber M, Weirich G, Panchal P, Gopalan A, Zurita J, Achilefu S, Chiosis G, Ponomarev V, Schwaiger M, Carver BS, Pomper MG, Grimm J (2018) Correction: prostate-specific membrane antigen cleavage of vitamin B9 stimulates oncogenic signaling through metabotropic glutamate receptors. J Exp Med 215:377
51. Colombatti M, Grasso S, Porzia A, Fracasso G, Scupoli MT, Cingarlini S, Poffe O, Naim HY, Heine M, Tridente G, Mainiero F, Ramarli D (2009) The prostate specific membrane antigen regulates the expression of IL-6 and CCL5 in prostate tumour cells by activating the MAPK pathways. PLoS One 4:e4608
52. Prima V, Kaliberova LN, Kaliberov S, Curiel DT, Kusmartsev S (2017) COX2/mPGES1/PGE2 pathway regulates PD-L1 expression in tumor-associated macrophages and myeloid-derived suppressor cells. Proc Natl Acad Sci U S A 114:1117–1122
53. Huang H, Wang C, Liu F, Li HZ, Peng G, Gao X, Dong KQ, Wang HR, Kong DP, Qu M, Dai LH, Wang KJ, Zhou Z, Yang J, Yang ZY, Cheng YQ, Tian QQ, Liu D, Xu CL, Xu DF, Cui XG, Sun YH (2018) Reciprocal network between cancer stem-like cells and macrophages facilitates the progression and androgen deprivation therapy resistance of prostate cancer. Clin Cancer Res 24:4612–4626. https://doi.org/10.1158/1078-0432.CCR-18-0461
54. Sun X, Gao D, Gao L, Zhang C, Yu X, Jia B, Wang F, Liu Z (2015) Molecular imaging of tumor-infiltrating macrophages in a preclinical mouse model of breast cancer. Theranostics 5:597–608
55. Movahedi K, Schoonooghe S, Laoui D, Houbracken I, Waelput W, Breckpot K, Bouwens L, Lahoutte T, de Baetselier P, Raes G, Devoogdt N, van Ginderachter JA (2012) Nanobody-based targeting of the macrophage mannose receptor for effective in vivo imaging of tumor-associated macrophages. Cancer Res 72:4165–4177
56. Locke LW, Mayo MW, Yoo AD, Williams MB, Berr SS (2012) PET imaging of tumor associated macrophages using mannose coated ^{64}Cu liposomes. Biomaterials 33:7785–7793
57. Perez-Medina C, Tang J, Abdel-Atti D, Hogstad B, Merad M, Fisher EA, Fayad ZA, Lewis JS, Mulder WJM, Reiner T (2015) PET imaging of tumor-associated macrophages with ^{89}Zr-labeled high-density lipoprotein nanoparticles. J Nucl Med 56:1272–1277
58. Tucker EW, Pokkali S, Zhang Z, DeMarco VP, Klunk M, Smith ES, Ordonez AA, Penet MF, Bhujwalla Z, Jain SK, Kannan S (2016) Microglia activation in a pediatric rabbit model of tuberculous meningitis. Dis Model Mech 9:1497–1506
59. Conway RE, Petrovic N, Li Z, Heston W, Wu D, Shapiro LH (2006) Prostate-specific membrane antigen regulates angiogenesis by modulating integrin signal transduction. Mol Cell Biol 26:5310–5324